Int. J. of Precis. Eng. and Manuf.-Green Tech.
https://doi.org/10.1007/s40684-026-00848-y

Online ISSN 2198-0810
Print ISSN 2288-6206

REGULAR PAPER

# Gradient Micro-Nano Structuring and Surface Enhancement of Aluminum Alloy through Nondestructive Femtosecond Laser Peening

**Pengjie Wang**[1,2,3] · **Haimin Ding**[1,2,3] · **Qing Peng**[4]

Received: 14 April 2025 / Revised: 10 December 2025 / Accepted: 14 January 2026


## Abstract

Modifying the top-layer surface microstructures represents a promising strategy for surface strengthening and is increasingly utilized in metal surface engineering. Here, we achieved nearly nondestructive surface reinforcement and gradient structuring of aluminum alloy using a low-energy femtosecond laser peening technique. Gradient micro-nano structures were formed after femtosecond laser peening treatment including gradient grains in size from hundreds of nanometers to a few micrometers, massive subgrain boundaries, various dislocation patterns, accompanied with more than one-fold elevated surface hardness and approximately unchanged surface evenness. The use of low pulse energy effectively suppresses thermal melting and collateral damage, ensuring high surface integrity. Atomistic simulations of defect evolution, such as dislocation propagation, multiplication, interactions with voids, and grain boundaries, demonstrate that ultrafast shockwaves facilitate the development of micro-nano structures, thereby enhancing the deformation capacity of the lattice and significantly improving the mechanical properties of the laser-treated surface. This advancement in metallic surface engineering techniques offers vast potential for manufacturing advanced metal materials with exceptional mechanical performance.

## Graphical Abstract

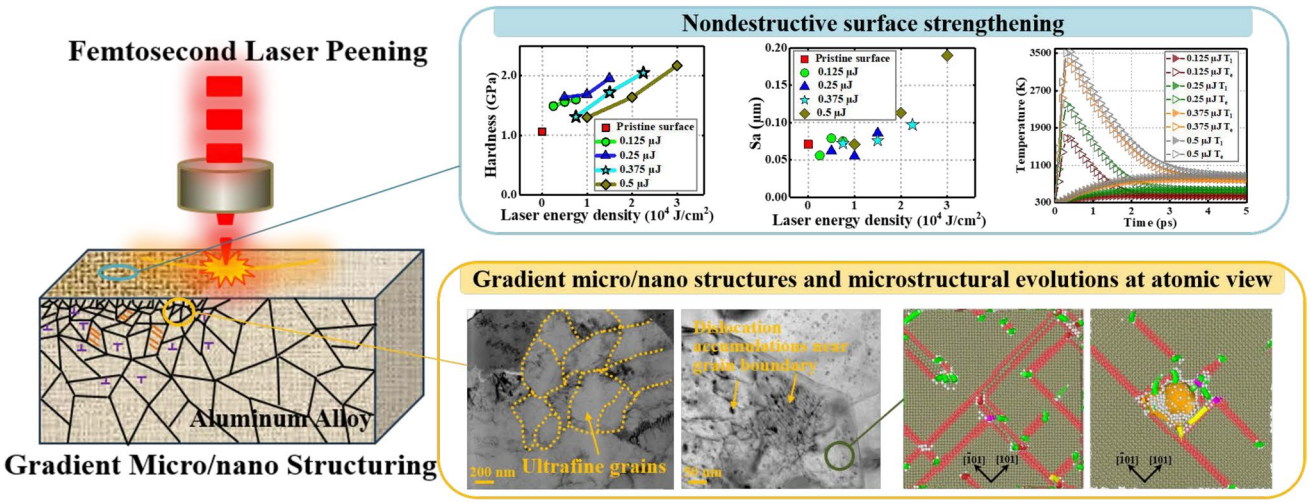


**Keywords** Femtosecond laser peening · Surface strengthening · Gradient structuring

Extended author information available on the last page of the article

Published online: 10 February 2026

## 1 Introduction

Strengthening metal matrices typically leads to a reduction in ductility, known as the strength-ductility trade-off, which limits the industrial applications of hard metallic materials. To address this challenge, various technological approaches have been proposed, including the optimization of micro/nano structures through dislocation architecture, nanotwin engineering, and gradient structuring [1]. Gradient metals with tunable microstructure distributions have demonstrated remarkable mechanical properties and achieved a synergy between strength and ductility, garnering significant research interest over the past two decades [2]. For example, a gradient dislocation-cell-structured alloy has shown an exceptional strain hardening rate at cryogenic temperatures, surpassing that of coarse-grained counterparts due to atomic-scale planar deformation faulting [3]. Additionally, gradient micro/nano structuring has achieved both superior strength and plasticity in various engineering metal materials [4–6]. Notably, a gradient nanograined surface layer can effectively reduce the coefficient of friction by accommodating substantial plastic deformation [7].

Several deformation pathways have been developed to fabricate gradient structures, including surface mechanical grinding, attrition, and rolling [2]. In contrast to these mechanical methods for inducing gradient plastic strain, laser shock peening represents an advanced technique for metallic surface reinforcement and gradient structure formation, offering advantages such as noncontact, repeatability, and precise control [8]. Traditional laser shock peening relies on high-energy nanosecond laser pulses to ablate a sacrificial coating within a confined liquid medium, generating a plasma shockwave that propagates into the substrate. This process introduces deep compressive residual stresses and gradient microstructures, leading to significant improvements in surface strength, fatigue life, wear, and corrosion resistance [9–11]. Although conventional nanosecond laser peening can achieve shock depths of hundreds of micrometers [9], it often results in surface damage and roughening on the order of tens of micrometers due to the combined action of thermal diffusion and shock wave impact [12, 13]. Therefore, achieving both high surface quality and enhanced performance remains a challenge for laser peening techniques.

Since its inception, femtosecond lasers have led to significant breakthroughs in fundamental physics and engineering sciences due to their ultrahigh peak intensity ($10^{13}$ W $cm^{-2}$). It provides another promising technological way to high-precision and high-quality surface strengthening of metal materials by applying the femtosecond lasers into laser peening field [14]. For instance, Zang et al. demonstrated surface strengthening and grain refinement in AZ31 magnesium alloy using femtosecond laser peening (FLP) without ablative or confinement layers [15]. Similarly, Trdan et al. applied FLP to AA2024-T3 aluminum alloy, reporting enhanced hardness and corrosion resistance due to microstructural refinement that suppressed intergranular attack [16]. Recent micro-diffraction experiments conducted by Rousseau et al. at a synchrotron source revealed FLP-induced depth profiles of residual stress and stored dislocation energy in an Al-0.3Mn alloy, confirming significant subsurface hardening [17]. However, Yu et al. compared the effects of high-energy nanosecond laser, low-energy nanosecond laser, and femtosecond laser peening, reporting that both low-energy nanosecond and femtosecond laser treatments resulted in limited peening effectiveness, which they attributed to thermally induced surface melting and oxidation [18].

Although femtosecond lasers have shown promise in recent laser peening applications, laser-induced thermal damage remains a major obstacle in practical engineering contexts. This limitation stems from the fact that current FLP processes typically follow the conventional nanosecond laser shock peening strategy—namely, a high-energy, single-pulse irradiation approach. Such a method often leads to surface thermal damage and nonuniform plastic deformation, substantially degrading surface finish and planarity. To address these challenges, we have developed an innovative FLP technique characterized by ultrahigh pulse density and ultralow pulse energy. In our previous studies, this approach enabled nondestructive surface enhancement in stainless steel and produced nano-gradient structures in Ti-6Al-4 V alloy [19, 20]. Notably, under ambient conditions without protective coating, this method enhanced surface hardness by more than 30% while maintaining nearly unchanged surface roughness [19]. These improvements are ascribed to the unique low-pulse-energy, high-pulse-density peening regime employed.

In the present study, we further elucidate the mechanisms underlying the surface nondestructive peening effect and subsurface micro/nano gradient structuring of aluminum alloy induced by femtosecond lasers, employing a comprehensive approach that integrates experimental techniques, finite element modeling, and molecular dynamics simulations. The enhancement of surface mechanical properties and the formation of micro/nano gradient structures at the top surface layer were characterized using nanoindentation and transmission electron microscopy (TEM), respectively. The evolution of thermal fields during laser-metal interactions was analyzed through finite element simulations coupled with the classical two-temperature equations. Molecular dynamics simulations were employed to elucidate the evolution of defects driven by femtosecond-laser induced ultrastrong shockwaves at a microscopic level.

## 2 Materials and Methods

### 2.1 Experimental Design

The FLP experiment was carried out at a femtosecond-laser micro/nano-machining workstation provided by Light Conversion, Lithuania. A Yb: KGW laser source (PHAROS) was employed for the FLP process, with central wavelength of 1026 nm, full-width at half-maximum (FWHM) around 190 fs, and repetition rate of 200 kHz. The ultrafast laser pulses were peened on sample surface without coating and confinement at normal incidence, after computer-controlled motorized attenuator and polarization rotation, focused by a microscope objective (5×, NA = 0.13, Olympus), yielding a laser facula of approximately 10 μm (Fig. 1a). A commercial 6061 aluminum alloy sample in $10 \times 10 \times 1$ mm$^3$ rectangular shape was mounted on a high-precision positioning stage with a movement accuracy less than 0.25 μm along all three axes. The sample surface was polished by SiC papers with roughness grades of 800#~3000# and cleaned in deionized water and ethanol under ultrasound prior to FLP treatment. The FLP process was monitored in real-time using a CCD device. Schematic illustration of the FLP process and laser scanning model were presented in Fig. 1c and d, respectively. Laser energy density was modulated by varying pulse density and pulse energy. In the experiments, four pulse energies (0.125, 0.25, 0.375, 0.5 μJ) and three pulse densities ($2 \times 10^8$, $4 \times 10^8$, $6 \times 10^8$ pulses/mm$^2$) were used, creating twelve distinct regions with varying laser parameters (Fig. 1b). The selection of these laser parameters is based on prior observations from femtosecond laser peening experiments on stainless steel [19], ensuring both surface integrity and effective peening. The low-energy and ultra-high-pulse-density peening model was conducted along the x-direction, with overlapping rate approximately 50% in the y-direction (Fig. 1d).

Displacement-controlled nanoindentation tests were conducted for the measurement of elastic modulus and surface hardness of aluminum alloy sample before and after FLP treatment, implemented with a Tl 950 Tribolndeter system (Hysitron lnc., USA). The Berkovich tip in radius of 50 nm was employed with a loading/unloading rate of 50 nm/s in nanoindentation tests. For each region treated by FLP, at least sixteen replicates were carried out at regular ordered spots. Elastic modulus and hardness were extracted from the

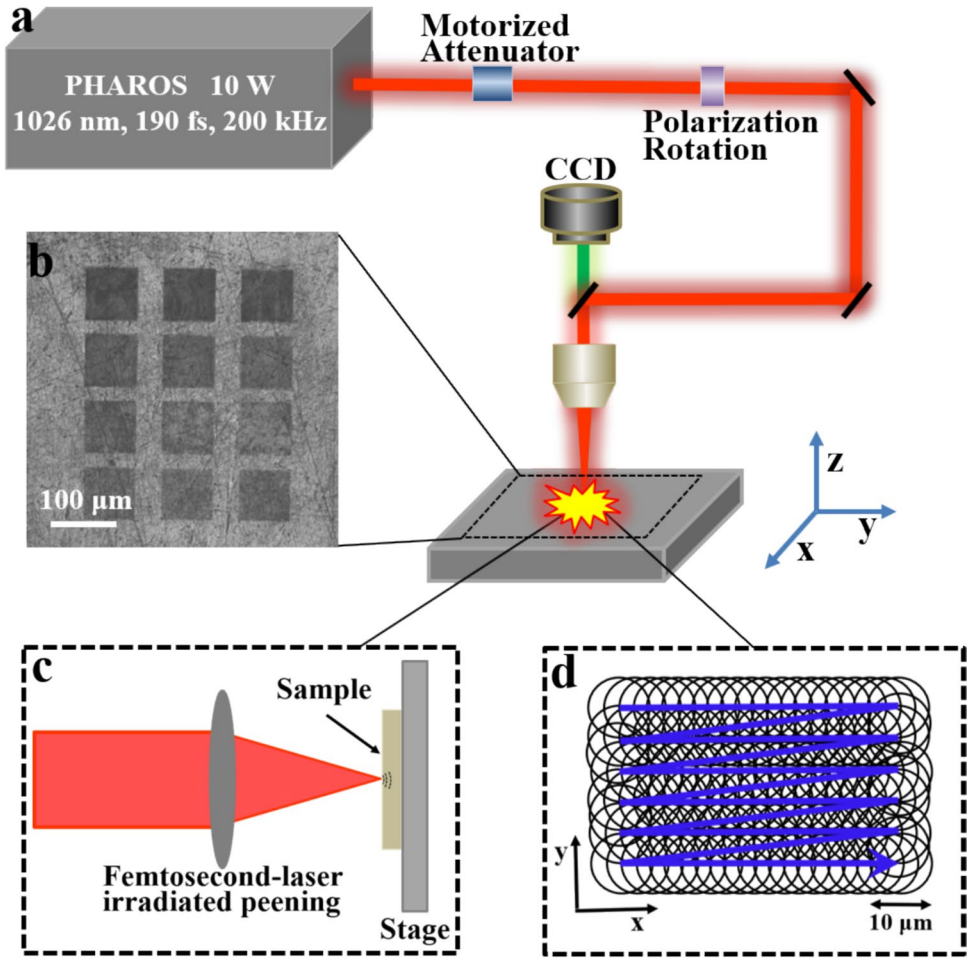


**Fig. 1** Experimental arrangement of the FLP process. (**a**) Optical setup of the femtosecond-laser machining system. (**b**) Optical image of aluminum-alloy sample surface after FLP treatment. (**c**) Schematic illustration of FLP and (**d**) laser scanning model

load–displacement relationships recorded in the tests based on Oliver-Pharr method [21].

Surface morphology and roughness measurement were performed by a 3D noncontact optical profilometer (NewView 9000, ZYGO Corp., USA), with a sub-nanometer accuracy at normal direction. Gradient micro/nanostructure at depth direction of the FLP-processed specimen were characterized via a JEM-F200 transmission electron microscope (TEM) operated at a voltage of 200 kV. TEM foil was prepared in thickness of approximately 100 nm by way of ion-beam cutting at depth direction on the FLP-processed surface.

### 2.2 Finite Element Analysis

A finite element numerical model incorporating two-temperature equations was developed to investigate the thermal dynamics of aluminum alloy surfaces treated with femtosecond lasers. Laser pulse energies ranged from 0.125 to 0.5 μJ, and the laser spot radius was set at 5 μm, consistent with experimental conditions. Femtosecond lasers with a pulse width of 200 fs were applied normal to the model surface. Adiabatic boundary conditions were implemented in the directions perpendicular to the laser incidence. The simulation employed a timestep of 5 fs, with a total simulation duration of 5 ps. The electron–phonon coupling constant for aluminum was set at $2.45 \times 10^{17}$ W $m^{-3}$ $K^{-1}$ [22]. Thermal field evolutions of electrons and lattice were computed using the two-temperature equations throughout the femtosecond laser acting processes.

### 2.3 Molecular Dynamic Simulations

The Large-scale Atomic/Molecular Massively Parallel Simulator (LAMMPS) package was employed for molecular dynamic (MD) simulations. Model size was $30 \times 300 \times 30$ $a_0^3$ in FCC atomic structure configuration with lattice constant ($a_0$) of 4.049 Å. A free boundary condition is applied in the shock direction, while periodic boundary condition was applied to the directions perpendicular to the laser shock wave. The embedded-atom-method (EAM) empirical potential was adopted to describe the interactions between aluminum atoms on account of its good applicability for metallic materials [23]. Laser shock effect was implemented by moving a piston to impact the atomic model (Fig. 4a) with piston velocities ranging from 0.5 to 3 km/s [24]. The initial instantaneous strain rate was in magnitude of $10^9$ $s^{-1}$ with piston velocity of 0.5—3 km/s. This is in good agreement with the strain rates experimentally measured during femtosecond laser ablation on aluminum [25], thereby validating the accuracy of our MD model. The timestep for the MD simulations was set to 0.5 fs. Ambient temperature was controlled around 300 K with Nosé–Hoover thermostat. Initially, the original atomic structure was adequately relaxed in succession within the isothermal-isobaric (NPT) and canonical (NVT) ensembles for 40 ps to equilibrate any pre-existing abnormal stresses. Following this, shock compression was applied within the microcanonical (NVE) ensemble, as the shock process is assumed to be adiabatic over the ultrashort timescale.

The OVITO package was used to analyze the defect evolutions during the laser peening process [26]. The atomic configurations were determined using the Common Neighbor Analysis (CNA) method, while dislocation features were characterized through Dislocation Analysis (DXA). The Von Mises Stress ($\sigma_{Mises}$) with a one-dimensional binning analysis was adopted to present the flow stress and identify the yield and dynamic plastic behaviors of the atomic structures. For each atom, $\sigma_{Mises}$ can be described by

$$\sigma_{Mises} = \frac{\sqrt{2}}{2}\sqrt{(\sigma_{xx}-\sigma_{yy})^2 + (\sigma_{yy}-\sigma_{zz})^2 + (\sigma_{xx}-\sigma_{zz})^2 + 6(\tau_{xy}^2 + \tau_{xz}^2 + \tau_{yz}^2)},$$

where $\sigma_{xx}$, $\sigma_{yy}$, $\sigma_{zz}$, $\tau_{xy}$, $\tau_{xz}$, $\tau_{yz}$ are the components of the calculated atomic stress, expressed as

$$\sigma_{\alpha\beta} = -\frac{1}{V}\left(\sum_i m_i v_{i\alpha} v_{i\beta} + \sum_i \sum_{i>j} r_{ij\alpha} f_{ij\beta}\right),$$

in which $m_i$ and $v_i$ are the mass and velocity of atom I, α and β denote x, y or z axes, $r_{ij}$ and $f_{ij}$ are the distance and force between atoms i and j, V is the atomic volume.

## 3 Results and Discussion

### 3.1 Surface Enhancement and Gradient Micro/nano Structures Induced by FLP

To balance effective peening-strengthening against excessive surface damage, we employed a low-energy, high-frequency FLP strategy using pulse energies between 0.125 and 0.5 μJ and an ultrahigh pulse density (~$10^8$ pulses/$mm^2$). After FLP treatment, the mechanical properties of the aluminum alloy surface were significantly enhanced (Figs. 2a, 2b). Surface hardening increased with laser energy density, accompanied by a modest rise in surface roughness (Fig. 2c, 2d). Critically, the combination of lower pulse energy with higher pulse density yielded superior surface enhancement, underscoring the advantage of the low-energy, high-frequency peening approach. Specifically, with a laser pulse energy of 0.5 μJ and a pulse density of $6 \times 10^8$ pulses/$mm^2$, the surface elastic modulus and hardness increased by 41% and 107%, respectively, compared to

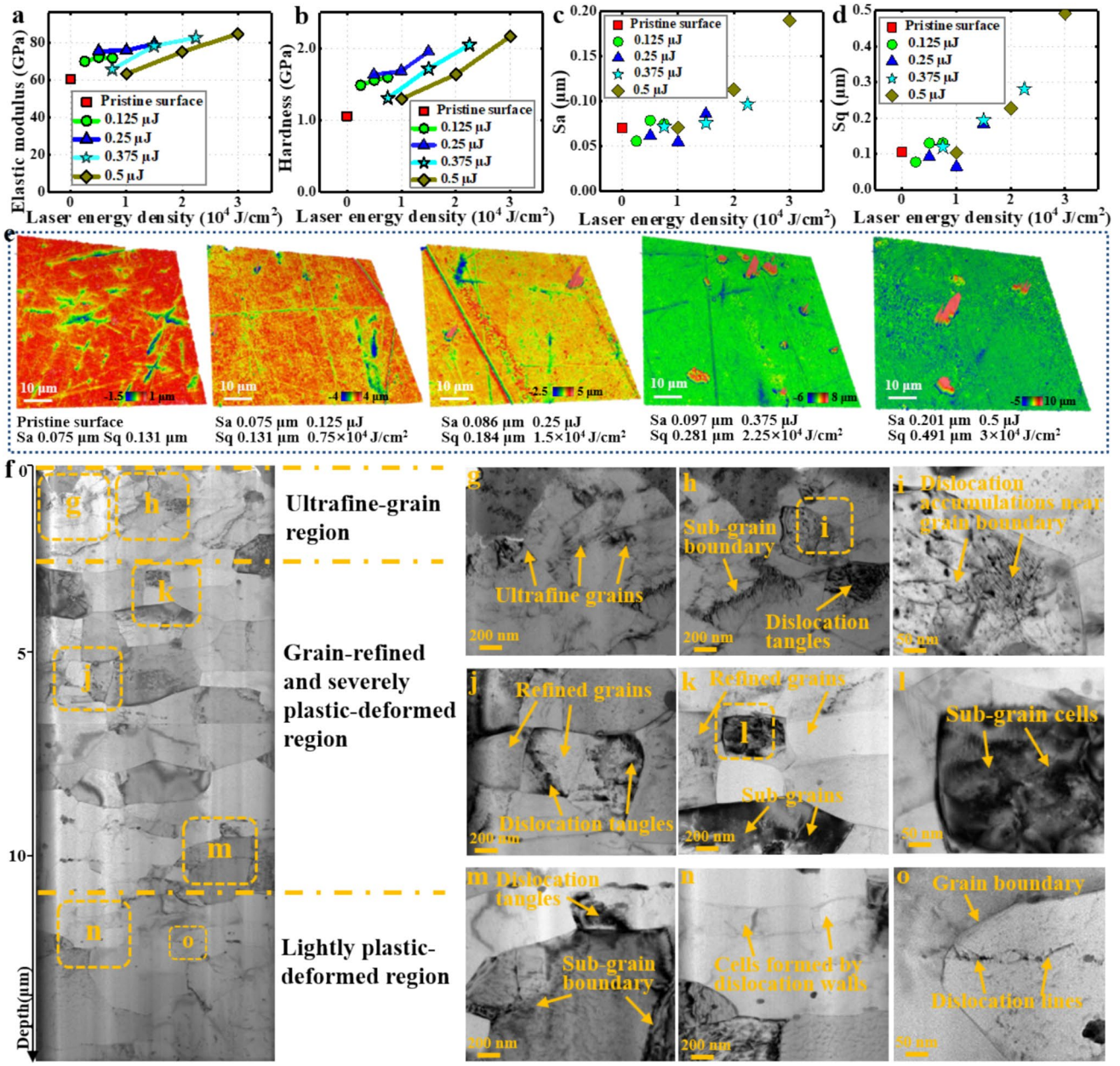


**Fig. 2** Surface integrity and micro-nano gradient structures at surface depth approximately 0 ~ 15 μm of 6061 aluminum alloy treated by low-energy femtosecond laser peening. (**a**) Elastic modulus, (**b**) surface hardness, (**c**) arithmetic mean deviation (Sa) and (**d**) root mean square deviation (Sq) of surface roughness versus laser energy density with pulse energies from 0.125 μJ to 0.5 μJ. (**e**) Morphologies of aluminum alloy surface with and without laser peening treatment. (**f**) Transmission electron microscopy image of gradient micro-nano structures at depth direction after laser peening treatment with a pulse energy of 0.5 μJ and a pulse density of $6 \times 10^8$ pulses/mm$^2$, including (**g, h**) ultrafine grains with sub-grain boundary and dislocation tangles at grain-refined region, (**i**) enlarged complex dislocation nano-patterns in (**h**), (**j, k**) refined grains with dislocation tangles near grain boundaries and intragranular sub grains at severe plastic-deformed region, (**l**) enlarged sub-grain cells in (**k**) formed by dislocation motion, (**m**) dislocation tangles connected with sub-grain boundaries, (**n, o**) mild dislocation motion and multiplication such as dislocation lines, dislocation cells, dislocation walls at slight plastic-deformed region

the pristine aluminum alloy surface, surpassing previously reported results [9, 16, 27].

In addition to the substantial surface reinforcement achieved through FLP technology, it also provides notable advantages in maintaining surface flatness. Compared to the original surface, the roughness of the laser-peened surface experiences minimal variation, remaining within the same order of magnitude. In most of our experiments, the roughness increment was less than a factor of one (Figs. 2c and 2d), a significant improvement compared to conventional nanosecond laser shock peening, which typically results in roughness increases exceeding tenfold [13, 27, 28]. This

finding underscores the high precision and low thermal impact associated with femtosecond laser peening. Figure 2e illustrates the topography of FLP-treated surfaces with varying laser energy densities alongside the pristine target surface. Unlike previous studies [29], this method did not induce laser-induced periodic structures on the peened surface. This is attributed to the use of low pulse energy combined with ultrahigh pulse density, which effectively minimizes thermal melting and maintains surface flatness during the FLP process.

Gradient micro/nano structures are renowned for their exceptional mechanical properties, including an outstanding strength-ductility synergy, high strength, and improved resistance to fatigue and corrosion [30–32]. However, manufacturing these gradient structures with high quality remains challenging due to the limitations of conventional mechanical methods, such as low precision and significant thermal effects [33], as well as the thermal damage associated with nanosecond laser shock peening [12]. Fortunately, the innovative low-energy FLP technology provides a promising solution to this challenge. Unlike conventional heat treatment processes such as annealing [34], which enhance plasticity and toughness at the expense of hardness, FLP enables significant grain refinement and the formation of gradient microstructures. It offers a precise, low-heat method for the high-quality fabrication of gradient micro/nano structures, addressing the limitations inherent in traditional methods and providing a potential solution to the longstanding strength-ductility trade-off in metallic materials [35].

Figure 2f depicts the gradient micro/nano structures along the depth direction, extending over a dozen micrometers. These structures are formed through ultrafast shock compression induced by femtosecond lasers and consist of an ultrafine-grain region, a grain-refined and severely plastically deformed region, and a lightly plastically deformed region. In contrast to the pristine aluminum alloy matrix Appendix, these regions display notable plastic deformation, characterized by pronounced grain refinement and a complex dislocation network. The gradient nature of these structures is closely linked to the attenuation of shock energy with increasing depth. For metal lattices with initial plastic deformation, dislocation motion predominantly governs the microstructural evolution. As the degree of plastic deformation increases, dislocation multiplication and accumulation lead to the formation of various dislocation structures, including dislocation walls, cells, tangles, and subgrain boundaries. Further plastic deformation promotes the transformation of subgrain boundaries into refined grain boundaries through continuous dynamic recrystallization [36]. Consequently, in the ultrafine-grain region near the peening surface, a high density of ultrafine grains, on the order of hundreds of nanometers, along with a high concentration of dislocations arranged in complex stacking patterns, are observed (Figs. 2g-i).

As the depth increases beyond 3 μm, large, refined grains ranging from hundreds of nanometers to several micrometers in size, along with severely accumulated dislocations, including stacking faults and dislocation tangles near the grain boundaries, are observed in the severely plastically deformed region (Figs. 2j and k). Notably, dislocation motion and intersection result in the formation of mesh-like nanostructures, generating numerous intragranular sub-grain cells, as shown in Fig. 2l. At the boundary of the severely plastically deformed region, a complex local nanostructure is formed, where subgrain boundaries are interconnected with dislocation tangles (Fig. 2m). This clearly reflects the dislocation processes, such as emission and propagation, occurring during the ultrafast shock compression. In the lightly plastically deformed region, extending over ten micrometers in depth, only mild dislocation motion and multiplication are observed, resulting in the formation of dislocation lines, walls, and cells, as illustrated in Figs. 2n and 2o.

The micro- and nano-structures formed are the primary contributors to the enhanced surface mechanical properties. Over recent decades, various technological approaches have been developed to tailor advanced microscale structures, including dislocation engineering, twinning design, and extreme grain refinement, to strengthen metals and overcome the strength-ductility trade-off [1]. Pre-existing dislocation architectures effectively inhibit dislocation motion and produce a pinning effect, thereby significantly improving the metal matrix's capacity to accommodate plastic deformation. Additionally, structural gradients exhibit remarkable mechanical properties compared to homogeneous materials due to their unique characteristics, such as strain delocalization and superior strain-hardening capabilities [5]. In homogeneous metals, strain localization arises from mismatches at grain boundaries, leading to nearly simultaneous plastic deformation across different grains. In contrast, gradient structures, with their orderly transition from coarse to finer grains, mitigate intergranular stress and suppress strain localization. This reduces crack formation and enhances fatigue resistance [35]. The work hardening associated with the accumulation of geometrically necessary dislocations in gradient-grain layers increases with the structural gradient and plastic strain gradient, contributing to additional strengthening and demonstrating an exceptional strength-ductility synergy [37].

### 3.2 Analysis of Thermal Fields During FLP Treatment

Minimizing thermal damage is paramount in ultrafast laser processing, as melting remains a primary driver of surface degradation that compromises the functional integrity of peened components. To elucidate and ultimately control the transient thermal fields, we employed a finite-element framework integrated with the classical two-temperature model. The two-temperature model, originally developed by Anisimov in the 1960s [38], accurately describes the temperature changes and energy transfer dynamics between electrons and lattices on ultrafast timescales. By integrating this model with the finite element method, we were able to visualize the temperature field evolutions during femtosecond laser peening.

As illustrated in Fig. 3a, a cylindrical domain (radius: 2 μm, height: 0.5 μm) was modeled. Under perpendicular irradiation by a 200-fs laser pulse, energy is first absorbed by free electrons via inverse bremsstrahlung within the first few hundred femtoseconds [39]. Subsequently, the metal lattice is gradually heated through electron–phonon coupling over several picoseconds. Figure 3b illustrates that the electron temperature field rapidly expands during the first 0.5 ps, followed by a gradual decrease. In contrast, the lattice temperature field evolves at a considerably slower rate. Figure 3c shows the electron–phonon dynamics predicted by the two-temperature model at the center of the laser-ablated region. The electron temperature peaks around 0.5 ps due to laser-electron interaction, then sharply declines as energy is transferred to the lattice. Meanwhile, the lattice temperature increases slowly until the conclusion of electron–phonon coupling. The distribution of electron and lattice temperatures along the depth and radius of the laser-irradiated region at various times is illustrated in Figs. 3d and 3e, respectively. The temperatures of electrons and lattices generally equilibrate after thermal conduction, irrespective of the direction (horizontal or vertical).

The peening effect arises from the explosion of plasmas, primarily involving material fragmentation and phase explosion induced by femtosecond laser interaction with the target surface [40]. According to femtosecond laser ablation mechanisms, even low-energy femtosecond lasers, with energies on the order of $10^{-1}$ μJ, can effectively induce material ejection and shock wave propagation in solids [41]. However, a temperature increase is an inevitable outcome of this process. Due to the relatively low laser intensity employed in our study, the peak temperature (850 K) of the aluminum lattice reached slightly below its melting point after electron–phonon coupling (Fig. 3b). This limitation prevented significant damage to the target surface through melting. Although heat accumulation occurs during the multipulse process, the constrained peak temperature inhibits large-scale thermal damage from melting phase transition.

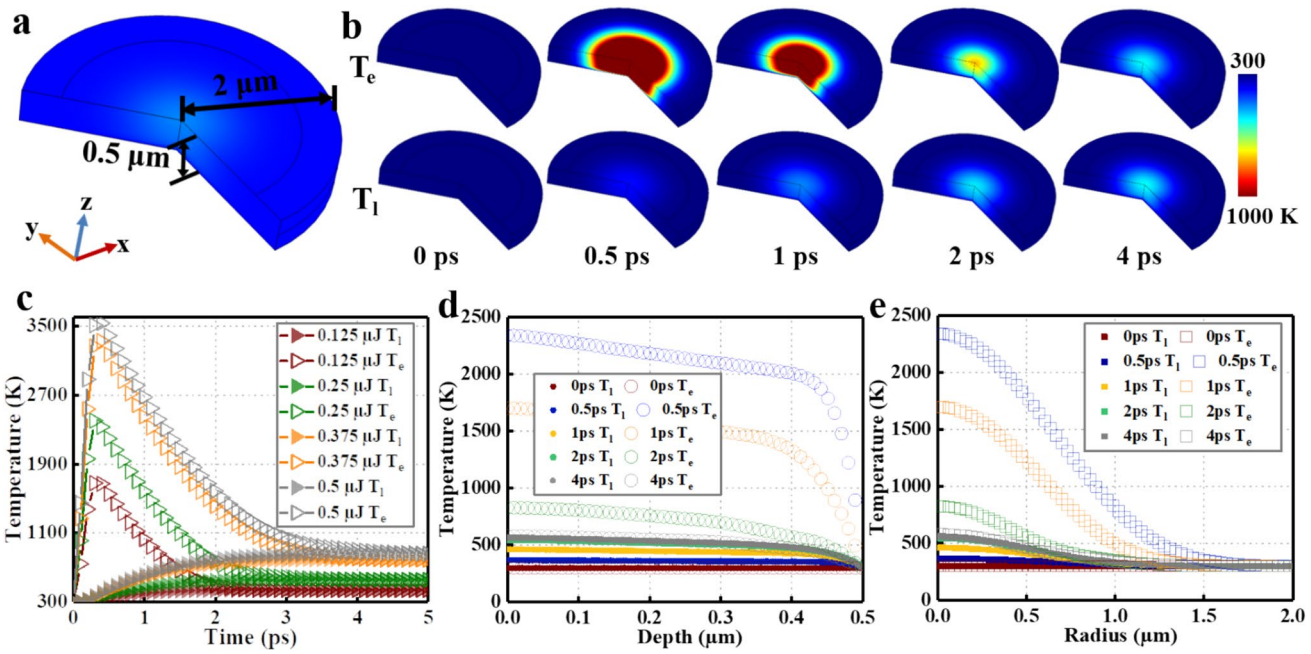


**Fig. 3** Evolutions of electron and lattice temperature fields during femtosecond laser acting on aluminum alloy predicted by two-temperature equations coupling with finite element model. (**a**) Aluminum alloy-based finite element model. (**b**) Temperature field evolutions of electrons and lattices in aluminum alloy-based finite element model with laser pulse energy of 0.25 μJ. (**c**) Electron–phonon coupling process versus time at laser-focused point with varied laser pulse energies. Electron temperature ($T_e$) and lattice temperature ($T_l$) distributions along (**d**) depth and (**e**) irradiated radius at different times. The hollow and solid points denote temperature of electrons and lattices, respectively

This characteristic is a primary reason for the exceptionally high surface quality achieved with low-energy femtosecond laser processing technology (Fig. 2c, d).

### 3.3 Defects Evolutions in Molecular Dynamic Perspective

Defect evolutions, such as the multiplication of dislocations and interstitials, interactions between different defects, are critical for accommodating plastic deformation induced by ultrafast compressive shock waves in metallic lattices. The capacity of metal lattices to sustain plastic deformation determines their yield limit and ultimate strength. Therefore, examining defect evolutions at a microscopic level, driven by laser-induced shock waves, is vital for understanding the alterations in the mechanical properties of the metal matrix. Figure 4a presents the atomic configuration of a molecular dynamic model with dimensions of $122 \times 12 \times 12$ nm$^3$. The classical piston method was employed to simulate shock compression, where a velocity was imparted to the piston to induce a shock effect on the atomic model [24]. Figure 4b depicts a typical cross-section of dislocation propagation at 7.5 ps, with the piston moving at a velocity of 1 km/s. At this initial stage, dislocations are generated and distributed in a regular pattern along the direction of the shock wave, owing to the limited range of shock energy propagation.

The propagation of shock waves can substantially alter the microstructure and atomic stress state [42]. Figures 4c-f illustrate the lattice's shock response over time, including the evolution of dislocations, atomic configurations, and flow stress. The motion of dislocations and the corresponding stress profile clearly demarcate distinct elastic and plastic zones, characterized by a leading elastic front followed by a plastic front [43]. In the plastic deformation regime, atomic stress increases rapidly until it reaches the yield point (plastic front), after which it remains elevated due to intense compression. However, this stress is lower than that observed in the elastic regime, as dislocation nucleation and motion dissipate the shock-induced shear stress. The stress fluctuations within the plastic region correspond to

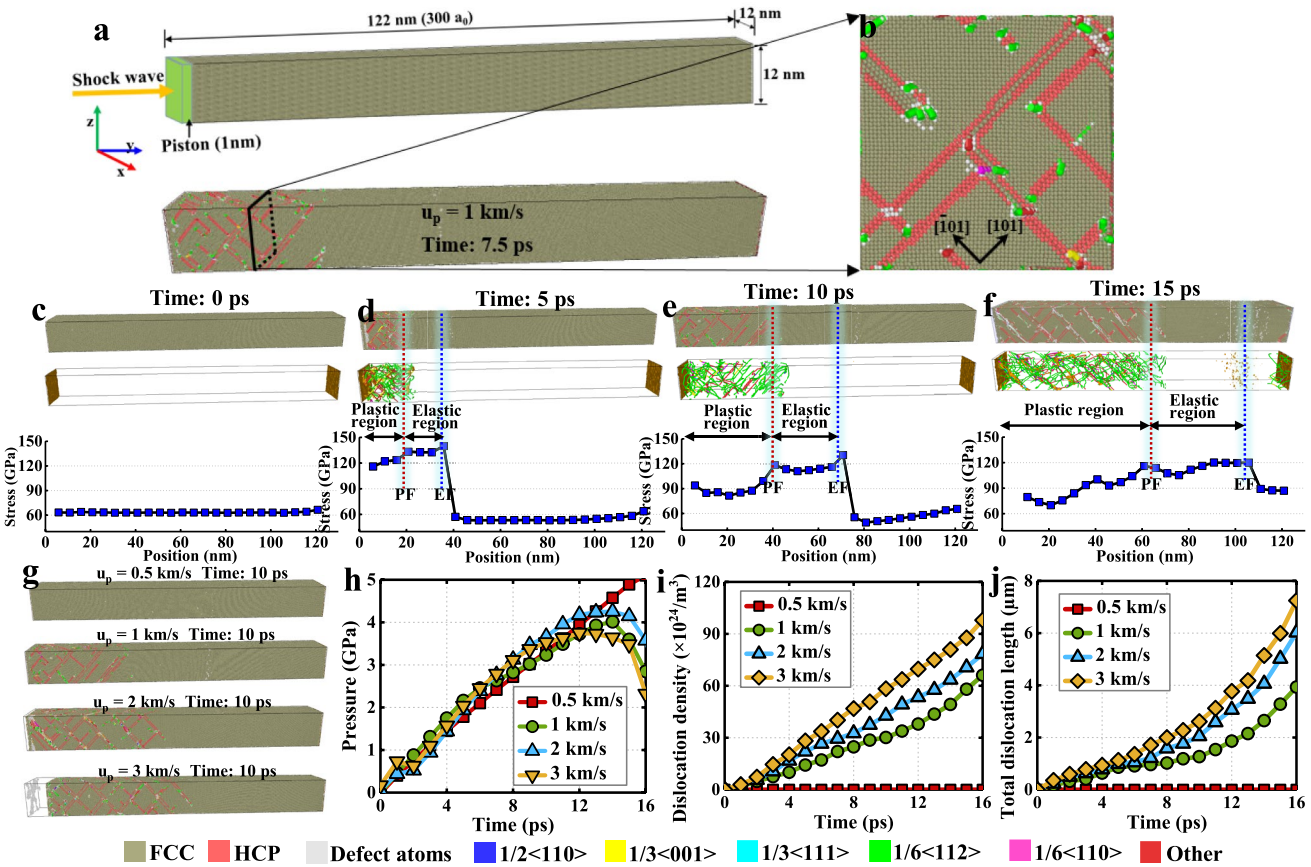


**Fig. 4** Dislocation evolutions during ultrafast compressive deformation via molecular dynamic simulations. (**a**) Molecular dynamic model in size of $30a_0 \times 300a_0 \times 30a_0$ with a piston in thickness of 1 nm. (**b**) Atomic configuration at cross-section and dislocation morphology at initial stage (time of 7.5 ps) with piston velocity of 1 km/s. (**c-f**) Dislocation motion and multiplication, as well as the flow stress distribution versus time. "EF" and "PF" denote elastic front and plastic front, respectively. (**g**) Contrast of atomic configurations at time of 10 ps with varied piston velocities. (**h**) Pressure at shock-loading direction ($\sigma_{yy}$), (**i**) dislocation density and (**j**) total dislocation length in MD model versus time with different piston velocities

the ongoing dislocation movement, with steady dislocation structures exhibiting a relatively lower flow stress. After surpassing the elastic front, atomic stress decreases sharply. As depicted in the atomic configurations, the evolution of flow stress and propagation of the plastic front along the shock loading direction are accompanied by the growth and interaction of dislocations, with a distinct crystallographic orientation dependence. Dislocation propagation and multiplication resulting in the formation of tangled dislocation networks, along with profuse point defect clusters, change the micro structural configuration and reinforce the lattice [42], reflecting the conversion of shock energy into lattice defect evolutions.

Shock intensity governs the loading strain rate and directly influences the evolution of defects and the subsequent reinforcement of the lattice. To explore how different shock intensities affect microstructural evolution, we employed a range of piston velocities in our simulations. Figure 4g presents the atomic snapshots at 10 ps for piston velocities spanning from 0.5 km/s to 3 km/s. As piston velocity and shock intensity increase, the rate of plastic deformation and dislocation slip accelerates significantly due to higher compressive strain rates. Figures 4h-j illustrate the pressure in shock-loading direction ($\sigma_{yy}$), dislocation density, and total dislocation length in the atomic model over time for various loading velocities. At a piston velocity of 0.5 km/s, the atomic model remains in the elastic deformation stage, characterized by increasing shock pressure but no observable yield point or dislocation formation (Fig. 4g), due to the relatively low shock intensity. In contrast, higher piston velocities lead to substantial promotion of dislocation motion and multiplication. It has been reported that stronger shock wave loading enhances dislocation mobility and extends dislocation structures, thereby dissipating excess shock energy [44]. According to the classical Taylor hardening law [45], the strength of metals increases with dislocation density. Consequently, diverse and stable dislocation configurations, such as dislocation forests [46], channels [47], and tangled cells [48], have been developed to reinforce the metal materials.

Defects such as voids and grain boundaries are prevalent in metallic materials. During mechanical deformation, interactions between various lattice defects, including dislocation-twinning reactions [49] and dislocation interactions with grain boundaries [50], are unavoidable. These interactions significantly influence metal strengthening, embrittlement, crack initiation, and strain hardening. To explore these interactions under ultrafast compressive shockwaves, we performed simulations with an atomic model incorporating pre-existing voids and grain boundaries, as illustrated in Fig. 5. Figures 5a-c show the flow stress and dislocation motion at different times for a piston velocity of 1 km/s in a lattice containing pre-existing voids. Notably, compared to a perfect lattice, a reduction in pressure along the shock direction is observed when the shockwave traverses the voids (Fig. 5d). Furthermore, the voids function as both barriers and sources for dislocations during plastic deformation (Fig. 5b, c), akin to solute segregation effects that enhance dislocation pinning and trapping [51]. This suggests that voids can absorb some shock energy and decelerate shockwave propagation by modifying dislocation evolution. Figures 5e and 5f present cross-sections at the void locations upon shockwave arrival, revealing that the voids effectively capture moving dislocations. Consequently, numerous dislocations nucleate at the void edges, leading to the formation of local complex nanostructures.

Grain boundaries are well-recognized as key barriers to dislocation movement, contributing to Hall–Petch strengthening [52, 53]. In addition, grain boundaries function as both sinks and sources, capable of absorbing and emitting dislocations [50]. This dual function is vividly captured in the atomic-scale model presented in Figs. 5g-l, which simulates an isolated grain boundary under ultrafast compressive loading. The model demonstrates how the grain boundary effectively arrests incoming dislocations, leading to the formation of pronounced dislocation pile-ups (Fig. 5i). Moreover, the morphology and distribution of dislocations differ markedly across the boundary (Fig. 5j), a consequence of the disparate crystallographic orientations in adjacent grains which govern local slip systems and dislocation evolution pathways. The increased dislocation pile-ups ahead of the grain boundary lead to higher back stress, which in turn enhances strain hardening [54]. Cross-sectional analysis at the atomic level (Fig. 5k) further reveals the grain boundary's role in absorbing and pinning a high density of dislocations. This process involves the accumulation of significant numbers of misoriented atoms, forming irregular defect meshes. By hindering dislocation movement, the grain boundary slows down the propagation of plastic deformation, thereby prolonging the elastically deformed phase of the lattice and generating greater compressive pressure in the shock direction compared to the perfect lattice scenario (Fig. 5l).

Those atomic-scale observations of nanostructure evolution driven by dislocation motion align well with experimental findings, such as dislocation propagation, pile-ups, and stacking at the pre-existing lattice defects (as displayed in Fig. 2). Effective strategies to enhance metal strength have historically focused on controlling dislocation multiplication, tangle formation, nanotwin development, and grain refinement [55, 56]. The elasticity and yield strength of metal lattices are governed by the deformation-bearing and plastic-deformation-carrying capacities of inherent lattice defects. Intense shock waves generated by femtosecond lasers produce extremely high peak pressures, supplying

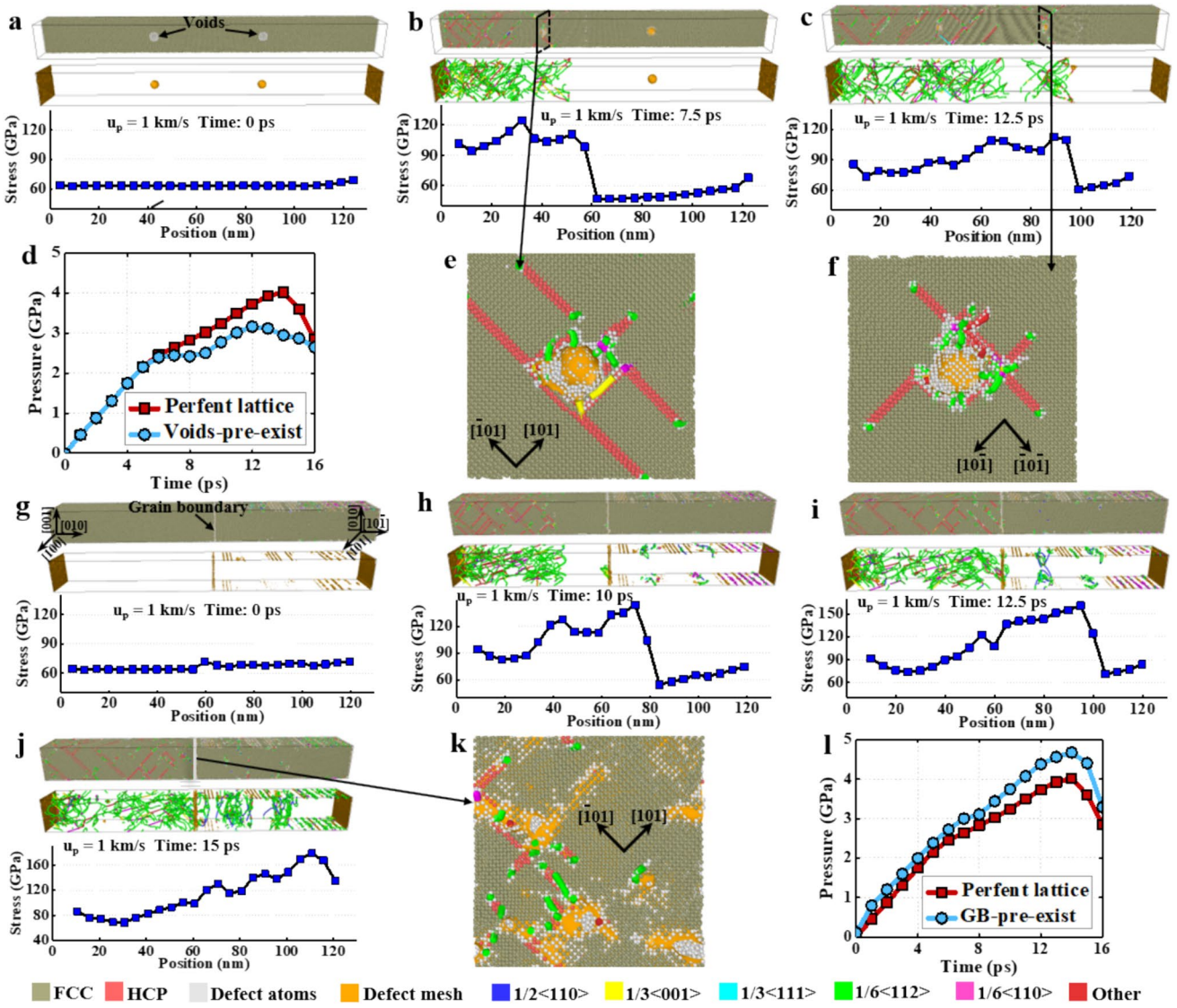


**Fig. 5** Effect of voids and grain boundary during ultrafast compressive deformation. (**a-c**) Atomic configurations, dislocation morphology and flow stress distribution at different times with piston velocity of 1 km/s at voids-pre-exist MD model. (**d**) Pressure at shock-loading direction ($\sigma_{yy}$) versus time in perfect and voids-pre-exist lattices. (**e**) and (**f**) show the atomic snapshots at cross-sections in region of the first and second voids, respectively. (**g-j**) Atom configurations, dislocation morphology and flow stress distribution at varied times of 0 ps, 10 ps, 12.5 ps and 15 ps with piston velocity of 1 km/s at grain-boundary-pre-exist MD model. (**k**) Atomic snapshot at cross-section of grain boundary. (**l**) Pressure at shock-loading direction versus time in perfect and grain-boundary-pre-exist lattices

sufficient energy to create numerous defect clusters and induce grain gradients. These clusters, predominantly comprising interstitials, vacancies, dislocations, and stacking faults, generate complex nanoscale stress fields that significantly enhance the metal lattice's carrying capacity. The formation of ultrafine grains and gradient micro/nano structures suppresses dislocation movement, improves strain localization, and activates various plastic deformation mechanisms under external loading [35]. Consequently, these processes effectively strengthen the mechanical properties of the bulk matrix at the surface level.

The low-energy femtosecond laser peening technique demonstrated in this study achieves a high-quality, nearly nondestructive surface strengthening, as evidenced in Figs. 1a-e. This superior outcome is attributed to two synergistic factors. First, the low single-pulse energy minimizes cumulative thermal damage, a critical advantage confirmed by our finite element simulations, which is essential for preserving surface integrity. Second, molecular dynamic simulations reveal that the ultrafast, ultrahigh-strain-rate compression in the surface layer triggers an explosive multiplication and entanglement of dislocations, leading to pronounced strain hardening. The experimentally observed

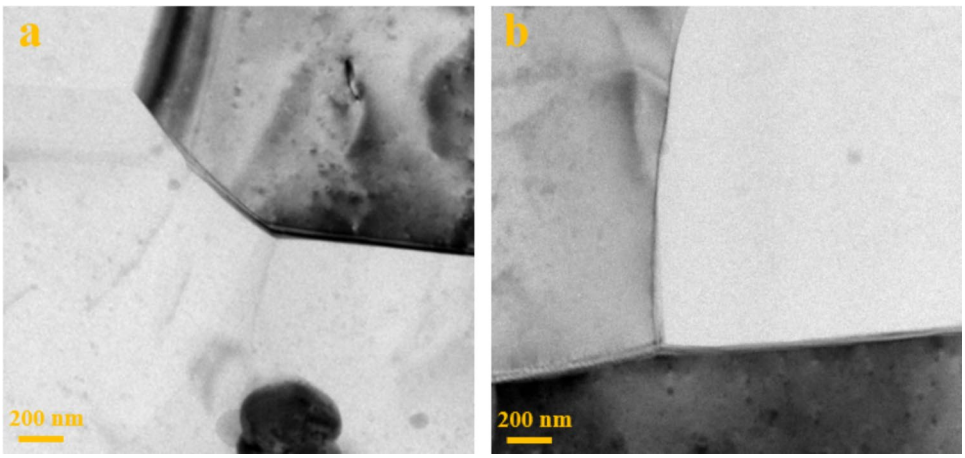


**Fig. 6** TEM images depicting the microstructures of pristine aluminum alloy

gradient micro-nano structures provide direct evidence of this evolving dislocation substructure. It is acknowledged that, constrained by computational scale, the present simulations do not fully capture the complete evolution of these gradient structures. Future work must prioritize cross-scale simulation methodologies to unravel the formation mechanisms of these complex gradient architectures on ultrafast timescales, thereby providing a more complete mechanistic understanding of the process.

## 4 Conclusions

We have successfully achieved surface enhancement and micro-nano gradient structuring on aluminum alloy surfaces using femtosecond laser peening without sacrificial overlays and confinement. The FLP treatment resulted in the formation of gradient structures, including gradient-distributed grains with sizes from hundreds of nanometers to a few micrometers, subgrain boundaries, and abundant dislocation morphologies. This treatment led to substantial increases in surface elastic modulus and hardness by 41% and 107%, respectively, while surface roughness remained minimally affected. These enhancements are attributed to the low-energy, high-pulse-density femtosecond laser peening method. Analysis of thermal fields indicates that the limited peak lattice temperatures during the low-energy femtosecond laser application prevent melting-induced thermal damage, thus ensuring the formation of a high-quality surface. Atomic-scale defect evolution studies reveal that dislocation propagation, pile-up, and interactions with other defects such as voids and grain boundaries significantly enhance the lattice's capacity to accommodate deformation, thereby substantially improving the mechanical performance of the laser-treated surface.

While initial progress has been made in achieving micro/nano structural gradients on aluminum alloy surfaces using low-energy FLP technology, significant challenges remain. Bridging the gap between understanding the fundamental mechanisms of gradient structuring under ultrafast compressive shockwaves and implementing effective surface enhancements on metal components with complex spatial structures necessitates advancements in experimental techniques and computational modeling, including in-situ and in-operando micro-observations. Future research should focus on optimizing laser parameters to achieve more profound grain refinement and tailored microstructural heterogeneity. Given its unique ability to manipulate microstructure formation in-situ, FLP technology offers significant potential for advancing high-performance metal additive manufacturing.

## Appendix:

(see Appendix Fig. 6).

**Acknowledgements** This work was financially supported by the Fundamental Research Funds for the Central Universities (No. 2025MS142), the National Natural Science Foundation of China (No. 52071142, 52001121 and 12272378), the Natural Science Foundation of Beijing (No. 2232065), Natural Science Foundation of Hebei Province (No. E2022502011 and E2022502004), and Strategic Priority Research Program of Chinese Academy of Sciences (No. XDB0620103).

**Author Contributions** P.W. conceived the idea, did the experiments, and wrote the paper. P.W., H.D. and Q.P. performed the data analysis and modified the draft. All the authors had full discussions and comments on the paper.

**Data Availability** All data generated or analyzed during this study are included in this published article.

## Declarations

**Conflicts of Interest** The authors declare no conflict of interest.

## References


1. Sun, L. G., Wu, G., Wang, Q., & Lu, J. (2020). Nanostructural metallic materials: Structures and mechanical properties. *Materials Today, 38*, 114–135. https://doi.org/10.1016/j.mattod.2020.04.005
2. Ji, W., Zhou, R., Viveganantha n, P., See Wu, M., Gao, H., & Zhou, K. (2023). Recent progress in gradient-structured metals and alloys. *Progress in Materials Science, 140*, Article 101194. https://doi.org/10.1016/j.pmatsci.2023.101194
3. Pan, Q., Yang, M., Feng, R., Chuang, A. C., An, K., Liaw, P. K., Wu, X., Tao, N., & Lu, L. (2023). Atomic faulting induced exceptional cryogenic strain hardening in gradient cell–structured alloy. *Science, 382*(6667), 185–190. https://doi.org/10.1126/science.adj3974
4. Pan, Q., Zhang, L., Feng, R., Lu, Q., An, K., Chuang, A. C., Poplawsky, J. D., Liaw, P. K., & Lu, L. (2021). Gradient cell–structured high-entropy alloy with exceptional strength and ductility. *Science, 374*(6570), 984–989. https://doi.org/10.1126/science.abj8114
5. Cheng, Z., Zhou, H., Lu, Q., Gao, H., & Lu, L. (2018). Extra strengthening and work hardening in gradient nanotwinned metals. *Science, 362*(6414), Article eaau1925. https://doi.org/10.1126/science.aau1925
6. Shao, C. W., Zhang, P., Zhu, Y. K., Zhang, Z. J., Tian, Y. Z., & Zhang, Z. F. (2018). Simultaneous improvement of strength and plasticity: Additional work-hardening from gradient microstructure. *Acta Materialia, 145*, 413–428. https://doi.org/10.1016/j.actamat.2017.12.028
7. Chen, X., Han, Z., Li, X., & Lu, K. (2016). Lowering coefficient of friction in Cu alloys with stable gradient nanostructures. *Science Advances, 2*(12), Article e1601942. https://doi.org/10.1126/sciadv.1601942
8. Deng, W., Wang, C., Lu, H., Meng, X., Wang, Z., Lv, J., Luo, K., & Lu, J. (2023). Progressive developments, challenges and future trends in laser shock peening of metallic materials and alloys: A comprehensive review. *International Journal of Machine Tools and Manufacture, 191*, Article 104061. https://doi.org/10.1016/j.ijmachtools.2023.104061
9. Fu, W., Huang, Y., Sun, J., & Ngan, A. H. W. (2022). Strengthening CrFeCoNiMn0.75Cu0.25 high entropy alloy via laser shock peening. *International Journal of Plasticity, 154*, Article 103296. https://doi.org/10.1016/j.ijplas.2022.103296
10. Chukwuike, V. I., Echem, O. G., Prabhakaran, S., AnandKumar, S., & Barik, R. C. (2021). Laser shock peening (LSP): Electrochemical and hydrodynamic investigation of corrosion protection pre-treatment for a copper surface in 3.5 % NaCl medium. *Corrosion Science, 179*, Article 109156. https://doi.org/10.1016/j.corsci.2020.109156
11. Feng, X., Pan, X., He, W., Liu, P., An, Z., & Zhou, L. (2021). Improving high cycle fatigue performance of gas tungsten arc welded Ti6Al4V titanium alloy by warm laser shock peening. *International Journal of Fatigue, 149*, Article 106270. https://doi.org/10.1016/j.ijfatigue.2021.106270
12. Sharma, A., Song, J., Furfari, D., Mannava, S. R., & Vasudevan, V. K. (2021). Remarkable near-surface microstructure of nanoparticles and oxide film in laser shock peened Al-Zn-Mg-Cu alloy. *Scripta Materialia, 202*, Article 114012. https://doi.org/10.1016/j.scriptamat.2021.114012
13. Wang, M., Chen, X., Dai, F., Siddiquee, A. N., & Konovalov, S. (2024). Effects of different laser shock processes on the surface morphology and roughness of TC4 titanium alloy. *Journal of Materials Processing Technology, 325*, Article 118301. https://doi.org/10.1016/j.jmatprotec.2024.118301
14. Wang, P., Zhou, J., Qi, F., Kong, X., & Ding, H. (2025). Progress in Femtosecond Laser Peening: Features, Applications and Development Prospects. *International Journal of Precision Engineering and Manufacturing-Green Technology*. https://doi.org/10.1007/s40684-025-00729-w
15. Zang, T., Wang, Z., Chen, L., Kong, M., Gao, S., Ngwangwa, H. M., Zhu, L., Yu, W., & Zheng, H. (2023). Influence of pulse energy on surface integrity of AZ31 magnesium alloy processed by femtosecond laser shock peening. *Journal of Materials Research and Technology, 25*, 4425–4440. https://doi.org/10.1016/j.jmrt.2023.06.227
16. Trdan, U., Sano, T., Klobčar, D., Sano, Y., Grum, J., & Šturm, R. (2018). Improvement of corrosion resistance of AA2024-T3 using femtosecond laser peening without protective and confining medium. *Corrosion Science, 143*, 46–55. https://doi.org/10.1016/j.corsci.2018.08.030
17. Rousseau, L., Iabbaden, D., Sedao, X., Peillon, N., Kalácska, S., & Lawrence Bright, E. (2025). Subsurface hardening of Al irradiated with ultrafast infrared laser. *Scripta Materialia, 255*, Article 116404. https://doi.org/10.1016/j.scriptamat.2024.116404
18. Yu, S., Ning, C., Wu, H., Li, Z., Wu, Y., & Cai, Z. (2025). Comparison of surface integrity, microstructure and corrosion resistance of Zr-4 alloy with various laser shock peening treatments. *Surface and Coatings Technology, 498*, Article 131799. https://doi.org/10.1016/j.surfcoat.2025.131799
19. Wang, P., Cao, Q., Liu, S., & Peng, Q. (2021). Surface strengthening of stainless steels by nondestructive laser peening. *Materials & Design, 205*, Article 109754. https://doi.org/10.1016/j.matdes.2021.109754
20. Wang, P., Ding, H., & Peng, Q. (2024). Nano gradient structuring at Ti-6Al-4V surface induced by ultrashort-pulse laser peening. *Journal of Manufacturing Processes, 132*, 105–111. https://doi.org/10.1016/j.jmapro.2024.10.083
21. Oliver, W. C., & Pharr, G. M. J. (1992). W C. Oliver, An Improved Technique for Determining Hardness and Elastic Modulus Using Load and Displacement Sensing Indentation. *Journal of Materials Research, 7*, 1564–1583.
22. Fernandez-Pañella, A., Ogitsu, T., Engelhorn, K., Correa, A. A., Barbrel, B., Hamel, S., Prendergast, D. G., Pemmaraju, D., Beckwith, M. A., Bae, L. J., Lee, J. W., Cho, B. I., Heimann, P. A., Falcone, R. W., & Ping, Y. (2020). Reduction of electron-phonon coupling in warm dense iron. *Physical Review B, 101*(18), Article 184309. https://doi.org/10.1103/PhysRevB.101.184309
23. Zhou, X. W., Wadley, H. N. G., Johnson, R. A., Larson, D. J., Tabat, N., Cerezo, A., Petford-Long, A. K., Smith, G. D. W., Clifton, P. H., Martens, R. L., & Kelly, T. F. (2001). Atomic scale structure of sputtered metal multilayers. *Acta Materialia, 49*(19), 4005–4015. https://doi.org/10.1016/S1359-6454(01)00287-7
24. Holian, B. L., & Lomdahl, P. S. (1998). Plasticity induced by shock waves in nonequilibrium molecular-dynamics simulations. *Science, 280*(5372), 2085–2088. https://doi.org/10.1126/science.280.5372.2085
25. Tamura, H., Kohama, T., Kondo, K., & Yoshida, M. (2001). Femtosecond-laser-induced spallation in aluminum. *Journal of Applied Physics, 89*(6), 3520–3522. https://doi.org/10.1063/1.1346996
26. Stukowski, A. (2009). Visualization and analysis of atomistic simulation data with OVITO–the Open Visualization Tool. *Modelling and Simulation in Materials Science and Engineering, 18*(1), Article 015012. https://doi.org/10.1088/0965-0393/18/1/015012
27. Dang, X., Liang, X., Luo, S., Li, Y., Jiao, Y., Tian, Z., & He, W. (2023). Surface strengthening and fatigue life improvement of single crystal Ni-based superalloys via laser shock peening without coating. *Materials & Design, 232*, Article 112097. https://doi.org/10.1016/j.matdes.2023.112097

28. Zhang, X., Liu, J., Xia, M., & Hu, Y. (2023). Laser shock peening enables 3D gradient metal structures: A case study on manufacturing self-armored hydrophobic surfaces. *International Journal of Machine Tools and Manufacture, 185*, Article 103993. https://doi.org/10.1016/j.ijmachtools.2023.103993
29. Pan, X., Zhou, L., Hu, D., He, W., Liu, P., Yu, Z., & Liang, X. (2023). Superior wear resistance in cast aluminum alloy via femtosecond laser induced periodic surface structures and surface hardening layer. *Applied Surface Science, 636*, Article 157866. https://doi.org/10.1016/j.apsusc.2023.157866
30. Wei, Y., Li, Y., Zhu, L., Liu, Y., Lei, X., Wang, G., Wu, Y., Mi, Z., Liu, J., Wang, H., & Gao, H. (2014). Evading the strength–ductility trade-off dilemma in steel through gradient hierarchical nanotwins. *Nature Communications, 5*(1), Article 3580. https://doi.org/10.1038/ncomms4580
31. Zou, J., Liang, Y., Jiang, Y., Yin, C., Huang, C., Liu, D., Zhu, Z., & Wu, Y. (2023). Fretting fatigue mechanism of 40CrNiMoA steel subjected to the ultrasonic surface rolling process: The role of the gradient structure. *International Journal of Fatigue, 167*, Article 107383. https://doi.org/10.1016/j.ijfatigue.2022.107383
32. Zou, J., Wang, Z., Ma, Y., Yan, Y., & Qiao, L. (2022). Role of gradient nano-structured surface in collapsed pitting corrosion on AISI 316L stainless steel during tribocorrosion. *Corrosion Science, 197*, Article 110043. https://doi.org/10.1016/j.corsci.2021.110043
33. Li, X., Lu, L., Li, J., Zhang, X., & Gao, H. (2020). Mechanical properties and deformation mechanisms of gradient nanostructured metals and alloys. *Nature Reviews Materials, 5*(9), 706–723. https://doi.org/10.1038/s41578-020-0212-2
34. Zhao, Y. H., Liao, X. Z., Jin, Z., Valiev, R. Z., & Zhu, Y. T. (2004). Microstructures and mechanical properties of ultrafine grained 7075 Al alloy processed by ECAP and their evolutions during annealing. *Acta Materialia, 52*(15), 4589–4599. https://doi.org/10.1016/j.actamat.2004.06.017
35. Lu, K. (2014). Making strong nanomaterials ductile with gradients. *Science, 345*(6203), 1455–1456. https://doi.org/10.1126/science.1255940
36. Lu, J. Z., Luo, K. Y., Zhang, Y. K., Cui, C. Y., Sun, G. F., Zhou, J. Z., Zhang, L., You, J., Chen, K. M., & Zhong, J. W. (2010). Grain refinement of LY2 aluminum alloy induced by ultra-high plastic strain during multiple laser shock processing impacts. *Acta Materialia, 58*(11), 3984–3994. https://doi.org/10.1016/j.actamat.2010.03.026
37. Cheng, Z., Bu, L., Zhang, Y., Wu, H., Zhu, T., Gao, H., & Lu, L. (2022). Unraveling the origin of extra strengthening in gradient nanotwinned metals. *Proceedings of the National Academy of Sciences, 119*(3), Article e2116808119. https://doi.org/10.1073/pnas.2116808119
38. Anisimov, S. (1966). Effect of powerful light fluxes on metals. *Zhurnal Tekhnicheskoi Fiziki, 36*, 1273–1283.
39. Turnbull, D., Katz, J., Sherlock, M., Divol, L., Shaffer, N. R., Strozzi, D. J., Colaïtis, A., Edgell, D. H., Follett, R. K., McMillen, K. R., Michel, P., Milder, A. L., & Froula, D. H. (2023). Inverse Bremsstrahlung absorption. *Physical Review Letters, 130*(14), Article 145103. https://doi.org/10.1103/PhysRevLett.130.145103
40. Zhang, N., Zhu, X., Yang, J., Wang, X., & Wang, M. (2007). Time-resolved shadowgraphs of material ejection in intense femtosecond laser ablation of aluminum. *Physical Review Letters, 99*(16), Article 167602. https://doi.org/10.1103/PhysRevLett.99.167602
41. Lorazo, P., Lewis, L. J., & Meunier, M. (2003). Short-pulse laser ablation of solids: From phase explosion to fragmentation. *Physical Review Letters, 91*(22), Article 225502. https://doi.org/10.1103/PhysRevLett.91.225502
42. Agarwal, G., Valisetty, R. R., & Dongare, A. M. (2020). Shock wave compression behavior and dislocation density evolution in Al microstructures at the atomic scales and the mesoscales. *International Journal of Plasticity, 128*, Article 102678. https://doi.org/10.1016/j.ijplas.2020.102678
43. Zhakhovsky, V. V., Budzevich, M. M., Inogamov, N. A., Oleynik, I. I., & White, C. T. (2011). Two-zone elastic-plastic single shock waves in solids. *Physical Review Letters, 107*(13), Article 135502. https://doi.org/10.1103/PhysRevLett.107.135502
44. Zhao, L., Zong, H., Ding, X., & Lookman, T. (2021). Anomalous dislocation core structure in shock compressed bcc high-entropy alloys. *Acta Materialia, 209*, Article 116801. https://doi.org/10.1016/j.actamat.2021.116801
45. Taylor, G. I. (1934). The mechanism of plastic deformation of crystals. Part I. Theoretical. *Proceedings of the Royal Society of London Series A, 145*(855), 362–387. https://doi.org/10.1098/rspa.1934.0106
46. He, B. B., Hu, B., Yen, H. W., Cheng, G. J., Wang, Z. K., Luo, H. W., & Huang, M. X. (2017). High dislocation density–induced large ductility in deformed and partitioned steels. *Science, 357*(6355), 1029–1032. https://doi.org/10.1126/science.aan0177
47. Lai, M. J., Tasan, C. C., & Raabe, D. (2015). Deformation mechanism of ω-enriched Ti–Nb-based gum metal: Dislocation channeling and deformation induced ω–β transformation. *Acta Materialia, 100*, 290–300. https://doi.org/10.1016/j.actamat.2015.08.047
48. Yu, H., Yan, M., Li, J., Godbole, A., Lu, C., Tieu, K., Li, H., & Kong, C. (2018). Mechanical properties and microstructure of a Ti-6Al-4V alloy subjected to cold rolling, asymmetric rolling and asymmetric cryorolling. *Materials Science and Engineering A, 710*, 10–16. https://doi.org/10.1016/j.msea.2017.10.075
49. Liebig, J. P., Krauß, S., Göken, M., & Merle, B. (2018). Influence of stacking fault energy and dislocation character on slip transfer at coherent twin boundaries studied by micropillar compression. *Acta Materialia, 154*, 261–272. https://doi.org/10.1016/j.actamat.2018.05.037
50. Kacher, J., Eftink, B. P., Cui, B., & Robertson, I. M. (2014). Dislocation interactions with grain boundaries. *Current Opinion in Solid State and Materials Science, 18*(4), 227–243. https://doi.org/10.1016/j.cossms.2014.05.004
51. Wang, Y. M., Voisin, T., et al. (2018). Additively manufactured hierarchical stainless steels with high strength and ductility. *Nature Materials, 17*(1), 63–71. https://doi.org/10.1038/nmat5021
52. Chokshi, A. H., Rosen, A., Karch, J., & Gleiter, H. (1989). On the validity of the hall-petch relationship in nanocrystalline materials. *Scripta Metallurgica, 23*(10), 1679–1683. https://doi.org/10.1016/0036-9748(89)90342-6
53. Hu, J., Shi, Y. N., Sauvage, X., Sha, G., & Lu, K. (2017). Grain boundary stability governs hardening and softening in extremely fine nanograined metals. *Science, 355*(6331), 1292–1296. https://doi.org/10.1126/science.aal5166
54. Zhang, X., Lu, S., Zhang, B., Tian, X., Kan, Q., & Kang, G. (2021). Dislocation–grain boundary interaction-based discrete dislocation dynamics modeling and its application to bicrystals with different misorientations. *Acta Materialia, 202*, 88–98. https://doi.org/10.1016/j.actamat.2020.10.052
55. Li, X., Wei, Y., Lu, L., Lu, K., & Gao, H. (2010). Dislocation nucleation governed softening and maximum strength in nano-twinned metals. *Nature, 464*(7290), 877–880. https://doi.org/10.1038/nature08929
56. Ke, X., Ye, J., Pan, Z., Geng, J., Besser, M. F., Qu, D., Caro, A., Marian, J., Ott, R. T., Wang, Y. M., & Sansoz, F. (2019). Ideal maximum strengths and defect-induced softening in nanocrystalline-nanotwinned metals. *Nature Materials, 18*(11), 1207–1214. https://doi.org/10.1038/s41563-019-0484-3

**Pengjie Wang** received his Ph.D. from Wuhan University in 2022. He is currently working as a researcher in the Department of Mechanical Engineering at North China Electric Power University. His current research fields include laser micro/nano processing, metal reinforcement, femtosecond-laser surface modification and additive manufacturing.

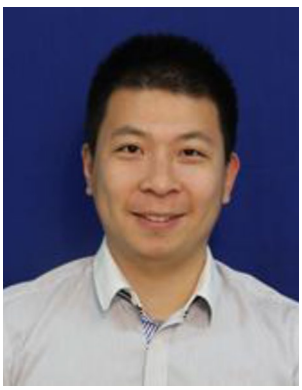

**Haimin Ding** is a Professor in the Department of Mechanical Engineering at North China Electric Power University. He received his Ph.D. from Shandong University. His research focuses on advanced structural materials and surface technology, especially high-temperature metal materials and their service performance.

**Qing Peng** is a Professor in School of Power and Mechanical Engineering, Wuhan University. He received his Ph.D. in physics from University of Connecticut in 2005, M.S. from Binghamton University, and B.S. from Peking University. His research focuses on materials physics and mechanics, especially radiation material science, using multiscale and first-principles computational modeling and simulation.

## Authors and Affiliations

**Pengjie Wang[1,2,3] · Haimin Ding[1,2,3] · Qing Peng[4]**

✉ Pengjie Wang
pjwang@ncepu.edu.cn

✉ Qing Peng
pengqing@whu.edu.cn

[1] Department of Mechanical Engineering, North China Electric Power University, Baoding 071000, China

[2] Hebei Key Laboratory of Electric Machinery Health Maintenance and Failure Prevention, North China Electric Power University, Baoding 071003, China

[3] Hebei Engineering Research Center for Advanced Manufacturing & Intelligent Operation and Maintenance of Electric Power Machinery, North China Electric Power University, Baoding 071003, China

[4] School of Power and Mechanical Engineering, Wuhan University, Wuhan 430072, China